

Memory of rotation in residual stress of paste

Hiroki Matsuda¹ and Michio Otsuki^{1,*}

¹*Graduate School of Engineering Science, Osaka University, Toyonaka 560-8531, Japan*

We numerically investigate the stress distribution in pastes after horizontal rotation by using an elasto-plastic model. Residual stress remains as a memory of rotation. The stress in the circumferential direction increases after the rotation, whereas that in the radial direction decreases. The residual stress is analytically related to the plastic deformation induced by the rotation. Based on the time evolution of plastic deformation, we theoretically describe the mechanism of the changes in the stress distribution.

I. INTRODUCTION

When a paste comprising water and powder is dried in a shallow container, cracks appear on its surface [1]. Crack patterns induced by desiccation are typically random and isotropic [2–6]. However, recent experiments have revealed that patterns become anisotropic when external fields are applied upon them [7–20]. In Refs. [7–9], it has been reported that the crack patterns on a paste made of calcium carbonate (CaCO_3) are controlled by horizontally oscillating the container before desiccation. When the paste is oscillated in a cylindrical container in one direction before desiccation, cracks perpendicular to the direction of the oscillation are formed, resulting in the lamellar crack pattern shown in Fig. 1 (a) [7]. In contrast, when the container was rotated horizontally in the angular direction, a radial crack pattern, as shown in Fig. 1 (b), is formed. Cracks are formed days after the oscillation, indicating that the paste memorizes the direction of the oscillation.

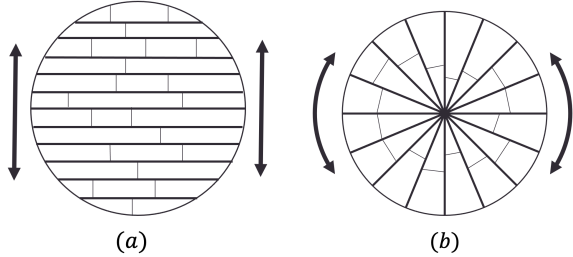


FIG. 1. Schematics of crack patterns on the surface of a paste in a cylindrical container. (a) The lamellar crack pattern after oscillation in one direction. (b) Radial crack pattern after oscillation in an angular direction. The thick lines represent the primary cracks formed initially. The thin lines represent the secondary cracks that are formed as desiccation progressed.

Pastes are elasto-plastic material characterized by the yield stress. According to Ref. [7], the memory effect occurs only when the stress induced by the oscillation exceeds the yield stress of the paste and causes plastic deformation. Therefore, the experimental results in Ref.

[7] suggest that the memory effect is related to the plastic deformation induced by oscillation. In fact, plastic deformation has been visualized in the paste showing the memory effect [21].

Cracks are formed when the tension in the paste is increased by desiccation and the fracture criterion is satisfied [1, 6, 22–31]. Hence, the memory effect is considered to result from a change in the tension or criterion. Recent experiments have revealed that desiccation does not change the criterion [32, 33]. This indicates that the tension induced by plastic deformation leads to the memory effect on the crack patterns. Therefore, understanding the mechanism of the residual stress after oscillation clarifies the origin of the memory effect.

In this respect, elasto-plastic models have been proposed to relate the residual stress to plastic deformation due to external oscillation in Refs. [34–37]. These models are used to study the plastic deformation of pastes after oscillation in one direction. In these models, the residual tension in the direction of oscillation increases owing to plastic deformation. Residual tension is enhanced by desiccation, creating lamellar crack patterns, as shown in Fig. 1(a) [34]. However, the models in the previous studies have been applied only to two-dimensional deformation in the vertical plane corresponding to lamellar crack patterns. Therefore, the mechanism for residual stress after horizontal rotation that leads to the radial crack pattern, as shown in Fig. 1(b), remains unclear.

In this study, we investigate the stress distribution of a paste in a cylindrical container rotated horizontally. We explain our setup and model in Sec. II. In Sec. II A, we introduce an elasto-plastic model for the paste. The boundary conditions and the choice of parameters are presented in Sec. II B. In Sec. III, we discuss residual stress after rotation. In Sec. III A, we show our numerical results, where the residual tension increases in the circumferential direction. Based on the time evolution of plastic deformation, we theoretically reveal the mechanism of increasing residual tension in Sec. III B. Finally, we conclude the study and discuss the results in Sec. IV.

II. SETUP

In this section, we first present the time evolution equations for a paste in a cylindrical container. We then

* m.otsuki.es@osaka-u.ac.jp

present the boundary conditions and parameters for the numerical simulation.

A. Elasto-plastic model

We consider a 3D elasto-plastic paste with a thickness of H in a cylindrical container with a diameter of D as shown in Fig. 2. Cartesian coordinates (x, y, z) are fixed to the container. The centre of the container is at $(x, y) = (0, 0)$ and the bottom at $z = 0$. The container is rotated at an angular velocity of $\boldsymbol{\Omega}(t)$.

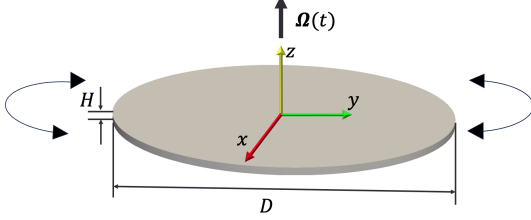


FIG. 2. Schematic of a paste in a cylindrical container rotated with angular velocity $\boldsymbol{\Omega}(t)$.

The configuration of the paste is represented by the current coordinates \mathbf{r} mapped from the initial coordinates $\mathbf{X} = (X, Y, Z)$ as follows:

$$\mathbf{r}(\mathbf{X}, t) = \begin{bmatrix} x(\mathbf{X}, t) \\ y(\mathbf{X}, t) \\ z(\mathbf{X}, t) \end{bmatrix}_{\text{C}}. \quad (1)$$

where $[\cdot]_{\text{C}}$ denotes the representation in Cartesian coordinates. Configuration $\mathbf{r}(\mathbf{X}, t)$ satisfies

$$\mathbf{r}(\mathbf{X}, t = 0) = \mathbf{X}. \quad (2)$$

The time evolution equation is given by [38–41]

$$\rho \frac{\partial^2 \mathbf{r}}{\partial t^2} = \text{div} \boldsymbol{\sigma} + \mathbf{f}, \quad (3)$$

where ρ denotes the density of the paste, \mathbf{f} is the body force, and $\boldsymbol{\sigma}$ is the Cauchy stress tensor. Here, $\boldsymbol{\sigma}$ consists of an elasto-plastic part $\boldsymbol{\sigma}^{(\text{EP})}$ and a viscous part $\boldsymbol{\sigma}^{(\text{V})}$ as follows:

$$\boldsymbol{\sigma} = \boldsymbol{\sigma}^{(\text{EP})} + \boldsymbol{\sigma}^{(\text{V})}. \quad (4)$$

The body force \mathbf{f} is generated by the rotation of the container as follows:

$$\mathbf{f} = -\rho \boldsymbol{\Omega} \times (\boldsymbol{\Omega} \times \mathbf{r}) - 2\rho \boldsymbol{\Omega} \times \dot{\mathbf{r}} - \rho \dot{\boldsymbol{\Omega}} \times \mathbf{r}, \quad (5)$$

where the first, second, and third terms represent the centrifugal, Coriolis, and Euler forces, respectively.

According to Ref. [37], we assume that the elasto-plastic part $\boldsymbol{\sigma}^{(\text{EP})}$ is given by

$$\boldsymbol{\sigma}^{(\text{EP})} = \{W + I_3 H'(I_3) + \mu\} \mathbb{1} + \mu(\mathbf{B} - \mathbb{1}) \quad (6)$$

with the left Cauchy-Green strain tensor \mathbf{B} . Here, W is the Hadamard strain energy [42]

$$W = \frac{1}{2} \{\mu(I_1 - 3) + H\} \quad (7)$$

with

$$H = (\lambda + \mu)(I_3 - 1) + 2(\lambda + 2\mu)(\sqrt{I_3 - 1}), \quad (8)$$

where λ and μ are the Lamé constants. Note that $I_1 = \text{tr} \mathbf{B}$ and $I_3 = \det \mathbf{B}$ are the rotation invariants of the left Cauchy-Green strain tensor. We assume $\lambda/\mu \gg 1$ to effectively realize the incompressibility of the paste. The viscous part, $\boldsymbol{\sigma}^{(\text{V})}$, is given by

$$\boldsymbol{\sigma}^{(\text{V})} = 2\eta \mathbf{S} \quad (9)$$

with the viscosity η and the stretching tensor \mathbf{S} [39].

The left Cauchy-Green tensor is defined as [39, 40]

$$\mathbf{B} = \mathbf{F} \mathbf{F}^{\text{T}} \quad (10)$$

with the deformation gradient tensor \mathbf{F} . The deformation gradient tensor \mathbf{F} represents the transformation of the infinitesimal line element $d\mathbf{r}$ between the two points labeled as \mathbf{X} and $\mathbf{X} + d\mathbf{X}$ from its local stress-free “natural state” $d\mathbf{r}^{\natural}$ as [37]

$$d\mathbf{r} = \mathbf{F} d\mathbf{r}^{\natural}. \quad (11)$$

The square of the distance between the two points is given by

$$|d\mathbf{r}|^2 = g_{ij} dX^i dX^j, \quad g_{ij} = (\partial_i \mathbf{r}) \cdot (\partial_j \mathbf{r}), \quad (12)$$

where the metric tensor is denoted by (g_{ij}) or \mathbf{g} . Here, we use $\partial_i = \partial/\partial X^i$ and the Einstein notation for the summation of the repeated indices. The square of the “natural distance” between the two points is given by

$$|d\mathbf{r}^{\natural}|^2 = g_{ij}^{\natural} dX^i dX^j, \quad (13)$$

where (g_{ij}^{\natural}) or \mathbf{g}^{\natural} is the natural metric tensor satisfying $g_{ij}^{\natural} = g_{ji}^{\natural}$.

The left Cauchy-Green tensor is represented by [37]

$$\mathbf{B} = g_{\natural}^{ij} (\partial_i \mathbf{r}) \otimes (\partial_j \mathbf{r}), \quad (14)$$

where (g_{\natural}^{ij}) or \mathbf{g}_{\natural} denotes the inverse of \mathbf{g}^{\natural} satisfying

$$\mathbf{g}_{\natural}^{\natural} \mathbf{g}_{\natural} = \mathbb{1}. \quad (15)$$

The stretching tensor \mathbf{S} is given by [37]

$$\mathbf{S} = -\frac{1}{2} (\partial_t g^{ij}) \{(\partial_i \mathbf{r}) \otimes (\partial_j \mathbf{r})\}, \quad (16)$$

where (g^{ij}) or \mathbf{g}^{-1} is the inverse of \mathbf{g} satisfying

$$\mathbf{g} \mathbf{g}^{-1} = \mathbb{1}. \quad (17)$$

Plastic deformation is characterized by the natural metric tensor. The natural metric tensor g_{ij}^{\natural} is initially set to $g_{ij}^{\natural} = \delta_{ij}$ at $t = 0$ and evolves when the equivalent stress $\bar{\sigma}$ exceeds the yield stress σ_Y . Following Refs. [35, 36], the time evolution of g_{ij}^{\natural} is given by

$$\tau \partial_t g_{ij}^{\natural} = \left(\Gamma g^{ij} - g_{ij}^{\natural} \right) \quad (18)$$

with a relaxation time τ and constant Γ , which is given by

$$\Gamma = \frac{3}{g^{ij} g_{ij}^{\natural}} \quad (19)$$

to satisfy the incompressibility condition $\det \mathbf{g}^{\natural} = 1$. The relaxation time is given by

$$\tau^{-1}(\bar{\sigma}) = \frac{\mu}{\eta_p} \max \left(0, 1 - \frac{\sigma_Y}{\bar{\sigma}} \right) \quad (20)$$

with a constant η_p [43]. The equivalent stress is given by

$$\begin{aligned} \bar{\sigma}^2 &= \frac{1}{2} (\sigma_{xx} - \sigma_{yy})^2 \\ &+ \frac{1}{2} (\sigma_{yy} - \sigma_{zz})^2 \\ &+ \frac{1}{2} (\sigma_{zz} - \sigma_{xx})^2 \\ &+ 3 (\sigma_{xy}^2 + \sigma_{yz}^2 + \sigma_{zx}^2), \end{aligned} \quad (21)$$

where σ_{ij} with $i, j = x, y, z$ is a component of the stress tensor. Equation (18) with Eq. (20) indicates that the plastic deformation associated with the change in (g_{ij}^{\natural}) occurs due to the finite relaxation time τ when the von Mises yield criterion $\bar{\sigma} \geq \sigma_Y$ is satisfied.

B. Boundary conditions and parameters

We introduce the cylindrical coordinates, where \mathbf{X} and \mathbf{r} are expressed as follows:

$$\mathbf{X} = \begin{bmatrix} R \cos \Theta \\ R \sin \Theta \\ Z \end{bmatrix}_{\mathbf{C}}, \quad \mathbf{r} = \begin{bmatrix} r \cos \theta \\ r \sin \theta \\ z \end{bmatrix}_{\mathbf{C}} \quad (22)$$

with

$$R = \sqrt{X^2 + Y^2}, \quad \Theta = \tan^{-1} \left(\frac{Y}{X} \right) \quad (23)$$

and

$$r = \sqrt{x^2 + y^2}, \quad \theta = \tan^{-1} \left(\frac{y}{x} \right). \quad (24)$$

We also introduce unit vectors

$$\mathbf{e}_r = \begin{bmatrix} \cos \theta \\ \sin \theta \\ 0 \end{bmatrix}_{\mathbf{C}}, \quad \mathbf{e}_{\theta} = \begin{bmatrix} -\sin \theta \\ \cos \theta \\ 0 \end{bmatrix}_{\mathbf{C}}, \quad \mathbf{e}_z = \begin{bmatrix} 0 \\ 0 \\ 1 \end{bmatrix}_{\mathbf{C}}. \quad (25)$$

We assume the no-slip boundary conditions $\partial_t \mathbf{r}(\mathbf{X}, t) = \mathbf{0}$ at the bottom of the container ($Z = 0$). The stress applied to the free surface at $Z = H$ is given by $\boldsymbol{\sigma} \mathbf{n} = \mathbf{0}$, where \mathbf{n} denotes the normal unit vector of the surface. At the lateral wall ($R = D/2$), we assume $\partial_t \mathbf{r}(\mathbf{X}, t) \cdot \mathbf{e}_r = 0$, $\mathbf{e}_{\theta} \cdot \boldsymbol{\sigma} \mathbf{e}_r = 0$, and $\mathbf{e}_z \cdot \boldsymbol{\sigma} \mathbf{e}_r = 0$, where the paste does not leave the wall and slides freely along the wall.

We oscillate the container N times in the angular direction with period T and relax the paste during a relaxation time T_R from the initial state. The angular velocity $\boldsymbol{\Omega}(t)$ is given by

$$\boldsymbol{\Omega} = \left[\begin{array}{c} 0 \\ 0 \\ \frac{d}{dt} \Phi(t) \end{array} \right]_{\mathbf{C}} \quad (26)$$

with the rotation angle

$$\Phi(t) = \begin{cases} A \cos \left(\frac{2\pi t}{T} \right) - 1 & (0 \leq t < NT) \\ 0 & (NT \leq t \leq NT + T_R) \end{cases} \quad (27)$$

and the amplitude A . We study the stress distribution after the rotation at $t = NT + T_R$.

We adopt $D/H = 50.0$, $\lambda/\mu = 1.0 \times 10^5$, $\eta/(\mu/\tau_0) = 1.0$, $\eta_p = 2.0\tau_0^{-1}$, and $\sigma_Y/\mu = 0.8$ with the unit of time $\tau_0 = H\sqrt{\rho/\mu}$ following the previous experiments [7] and simulations [37]. We set $T/\tau_0 = 5.0$, $A = 0.1$, $N = 10$, and $T_R/\tau_0 = 80.0$. Equation (3) is solved numerically by using the finite element method with a time step $\Delta t/\tau_0 = 2.0 \times 10^{-4}$. The paste is divided into cubes of length $\Delta x/D = 1.0 \times 10^{-2}$ consisting of six tetrahedrons. Note that we have checked that $N \geq 10$ and a longer T_R give the same results shown below.

III. RESIDUAL STRESS AFTER THE ROTATION

In this section, we first present the numerical results of the stress distribution after the rotation. Then, the mechanism of the residual stress is theoretically explained.

A. Distribution of the residual stress

We focus on the deviatoric stress

$$\mathbf{S} = \boldsymbol{\sigma} - \left(\frac{\text{tr} \boldsymbol{\sigma}}{3} \right) \mathbf{I} \quad (28)$$

because a crack is formed when \mathbf{S} becomes significant. We introduce the components of the deviatoric stress tensor in the cylindrical coordinates as follows:

$$S_{\alpha\beta} = \mathbf{e}_{\alpha} \cdot \mathbf{S} \mathbf{e}_{\beta} \quad (29)$$

with $\alpha, \beta = r, \theta, z$ and plot the spatial distributions of S_{rr} and $S_{\theta\theta}$ after rotation at the bottom ($Z = 0$) in

Figs. 3 and 4, respectively. The stress distributions exhibit rotational symmetry. S_{rr} and $S_{\theta\theta}$ are 0 near the centre of the system. However, in the outer region, the nonzero residual stress ($S_{rr} < 0$ and $S_{\theta\theta} > 0$) remains as a memory of the rotation even though the system is sufficiently relaxed after rotation. The magnitudes of S_{rr} and $S_{\theta\theta}$ increase with increasing R . The components S_{rr} and $S_{\theta\theta}$ represent the tension in the radial and circumferential directions, respectively. A positive value of $S_{\theta\theta}$ is consistent with the crack patterns shown in Fig. 1(b), where the radial cracks appear to release the increasing tension in the circumferential direction.

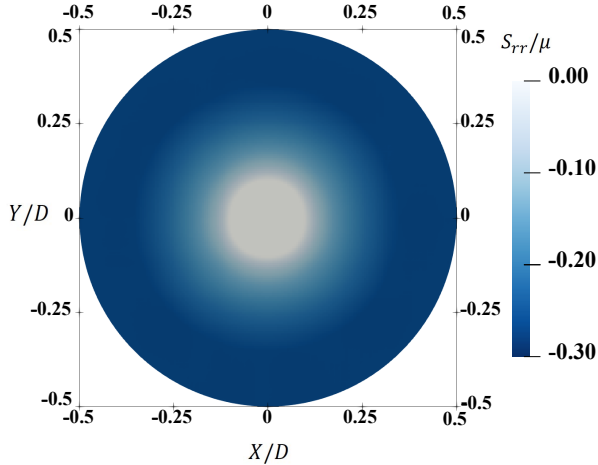


FIG. 3. Spatial distribution of S_{rr} at $Z = 0$ after the rotation.

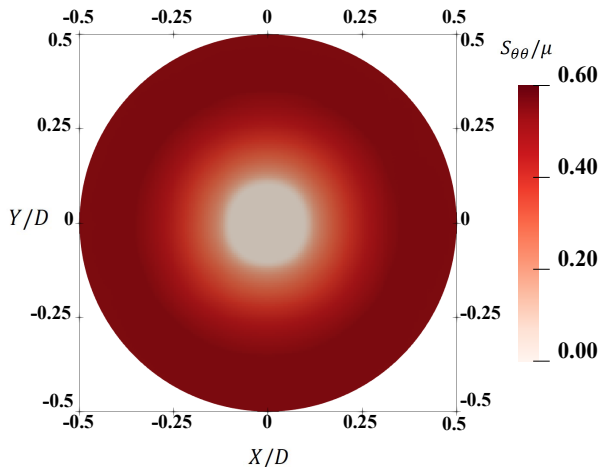


FIG. 4. Spatial distribution of $S_{\theta\theta}$ at $Z = 0$ after the rotation.

In Figs. 5 and 6, we plot the spatial distributions of S_{rr} and $S_{\theta\theta}$ after the rotation for $\Theta = 0$, respectively.

At $R = D/2$ and $z = H$, $|S_{rr}|$ and $|S_{\theta\theta}|$ are largest. In this system, the Euler force along the circumferential direction is dominant in Eq. (5) and induces large deformation near the wall. In addition, the shear stress becomes the largest near the bottom owing to the boundary conditions. Therefore, the equivalent stress becomes the largest at the bottom near the wall of the cylindrical container, where large plastic deformation and residual stress $S_{rr} < 0$ and $S_{\theta\theta} > 0$ occur.

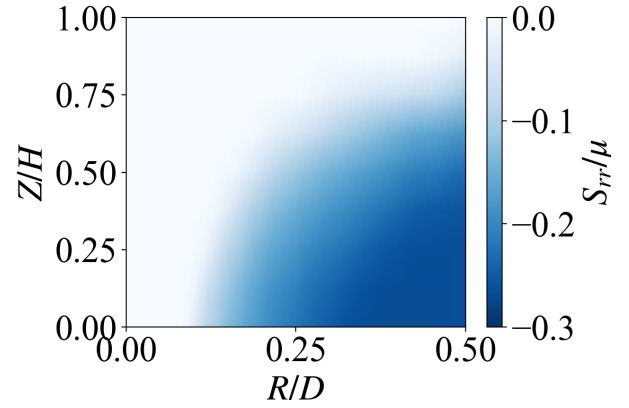


FIG. 5. Spatial distribution of S_{rr} for $\Theta = 0$ after the rotation.

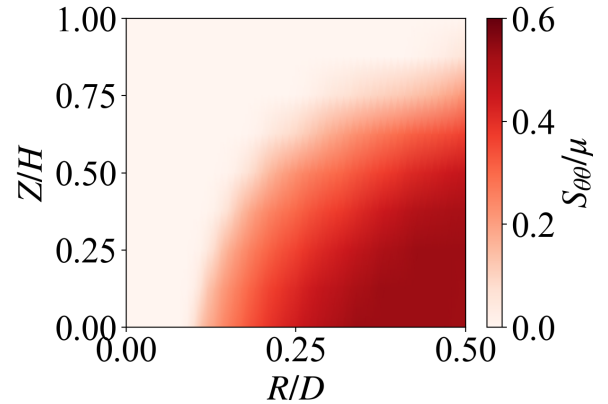


FIG. 6. Spatial distribution of $S_{\theta\theta}$ for $\Theta = 0$ after the rotation.

B. Theoretical explanation for residual stress

We theoretically analyze the origin of the negative S_{rr} and positive $S_{\theta\theta}$ after the rotation. Substituting Eq. (4) into Eq. (28) with Eq. (6), we obtain

$$\mathbf{S} = \mu \left(\mathbf{B} - \frac{\text{tr} \mathbf{B}}{3} \mathbf{I} \right), \quad (30)$$

where we have neglected $\boldsymbol{\sigma}^{(V)}$ by assuming quasi-static deformation. By substituting this equation into Eq. (29), S_{rr} and $S_{\theta\theta}$ can be expressed as follows:

$$S_{rr} = \mu \left(B_{rr} - \frac{B_{rr} + B_{\theta\theta} + B_{zz}}{3} \right), \quad (31)$$

$$S_{\theta\theta} = \mu \left(B_{\theta\theta} - \frac{B_{rr} + B_{\theta\theta} + B_{zz}}{3} \right) \quad (32)$$

with the components of the left Cauchy-Green tensor in the cylindrical coordinates

$$B_{\alpha\beta} = \mathbf{e}_\alpha \cdot \mathbf{B} \mathbf{e}_\beta. \quad (33)$$

The left Cauchy-Green tensor is determined using the natural metric tensor \mathbf{g}^{\natural} , which is expressed as

$$\mathbf{g}^{\natural} = \begin{pmatrix} g_{XX}^{\natural} & g_{XY}^{\natural} & g_{XZ}^{\natural} \\ g_{XY}^{\natural} & g_{YY}^{\natural} & g_{YZ}^{\natural} \\ g_{XZ}^{\natural} & g_{YZ}^{\natural} & g_{ZZ}^{\natural} \end{pmatrix} = \mathbf{Q}^T \mathbf{G}^{\natural} \mathbf{Q} \quad (34)$$

with the rotation matrix

$$\mathbf{Q} = \begin{pmatrix} \cos \theta & \sin \theta & 0 \\ -\sin \theta & \cos \theta & 0 \\ 0 & 0 & 1 \end{pmatrix}. \quad (35)$$

Here, $\mathbf{G}^{\natural} = \mathbf{Q} \mathbf{g}^{\natural} \mathbf{Q}^T$ is represented as

$$\mathbf{G}^{\natural} = \begin{pmatrix} 1 + \Delta G_{rr}^{\natural} & \gamma & \delta \\ \gamma & 1 + \Delta G_{\theta\theta}^{\natural} & \epsilon \\ \delta & \epsilon & \Xi \end{pmatrix}. \quad (36)$$

At $t = 0$, ΔG_{rr}^{\natural} , $\Delta G_{\theta\theta}^{\natural}$, γ , δ , and ϵ are 0, and plastic deformation is characterized by their time evolution. From the incompressible condition, $\det \mathbf{g}^{\natural} = \det \mathbf{G}^{\natural} = 1$, Ξ satisfies

$$\Xi = \frac{1 + \epsilon^2(1 + \Delta G_{rr}^{\natural}) + \delta^2(1 + \Delta G_{\theta\theta}^{\natural}) - 2\gamma\delta\epsilon}{(1 + \Delta G_{rr}^{\natural})(1 + \Delta G_{\theta\theta}^{\natural}) - \gamma^2}. \quad (37)$$

In our system, the Euler force causes the rigid rotation at each height Z . Therefore, we approximate the deformation of the paste as

$$r(\mathbf{X}, t) = R, \quad \theta(\mathbf{X}, t) = \Theta + \varphi(Z, t), \quad z(\mathbf{X}, t) = Z \quad (38)$$

with a rotation angle $\varphi(Z, t)$. In the analysis below, we consider the case of a small deformation with $\varphi \ll 1$ and neglect the higher-order terms of ΔG_{rr}^{\natural} , $\Delta G_{\theta\theta}^{\natural}$, γ , δ , ϵ , and \mathbf{G}^{\natural} . Using Eqs. (34), (36), and (38) with Eq. (14), we obtain

$$B_{rr} \simeq 1 - \Delta G_{rr}^{\natural}, \quad (39)$$

$$B_{\theta\theta} \simeq 1 - \Delta G_{\theta\theta}^{\natural}, \quad (40)$$

$$B_{zz} \simeq 1 + \Delta G_{rr}^{\natural} + \Delta G_{\theta\theta}^{\natural}. \quad (41)$$

Appendix A provides the derivation of these equations. Substituting Eqs. (39)-(41) into Eqs. (31) and (32), we obtain

$$S_{rr} \simeq -\mu \Delta G_{rr}^{\natural}, \quad (42)$$

$$S_{\theta\theta} \simeq -\mu \Delta G_{\theta\theta}^{\natural}. \quad (43)$$

These equations relate the plastic deformation characterized by ΔG_{rr}^{\natural} and $\Delta G_{\theta\theta}^{\natural}$ to the residual stress.

Based on Eqs. (18), (34), (36), and (38), we derive the time evolution equations of ΔG_{rr}^{\natural} and $\Delta G_{\theta\theta}^{\natural}$ as

$$\partial_t \Delta G_{rr}^{\natural} \simeq \tau^{-1} \left\{ \frac{1}{3} R^2 (\partial_Z \varphi)^2 - \Delta G_{rr}^{\natural} \right\}, \quad (44)$$

$$\partial_t \Delta G_{\theta\theta}^{\natural} \simeq \tau^{-1} \left\{ -\frac{2}{3} R^2 (\partial_Z \varphi)^2 - \Delta G_{\theta\theta}^{\natural} \right\}. \quad (45)$$

See Appendix B for details on the derivation. As the shear strain represented by $R(\partial_Z \varphi)$ increases owing to the rotation, the equivalent stress $\bar{\sigma}$ exceeds σ_Y and τ^{-1} becomes nonzero, which causes a change in ΔG_{rr}^{\natural} and $\Delta G_{\theta\theta}^{\natural}$. In Eqs. (44) and (45), ΔG_{rr}^{\natural} converges to $\frac{1}{3} R^2 (\partial_Z \varphi)^2 > 0$, while $\Delta G_{\theta\theta}^{\natural}$ changes to $-\frac{2}{3} R^2 (\partial_Z \varphi)^2 < 0$. After the rotation of the cylinder stops, positive ΔG_{rr}^{\natural} and negative $\Delta G_{\theta\theta}^{\natural}$ remain because τ^{-1} in Eqs. (44) and (45) become 0 before the rotation stops, which leads to the residual stress $S_{rr} < 0$ and $S_{\theta\theta} > 0$ through Eqs. (42) and (43). Note that Eq. (45) corresponds to the time evolution equation of the natural metric tensor in pastes oscillated in one direction in Ref. [35].

In Figs. 7 and 8, we plot the spatial distributions of ΔG_{rr}^{\natural} and $\Delta G_{\theta\theta}^{\natural}$ at $Z = 0$ after the rotation, respectively. The components ΔG_{rr}^{\natural} and $\Delta G_{\theta\theta}^{\natural}$ are 0 near the center of the container. As R increases, ΔG_{rr}^{\natural} increases from 0 and $\Delta G_{\theta\theta}^{\natural}$ decreases. The numerical results for $\Delta G_{rr}^{\natural} \geq 0$ and $\Delta G_{\theta\theta}^{\natural} \leq 0$ are consistent with the time evolutions described by Eqs. (44) and (45). The spatial distributions of ΔG_{rr}^{\natural} and $\Delta G_{\theta\theta}^{\natural}$ are consistent with those of S_{rr} and $S_{\theta\theta}$ in Figs. 3 and 4, respectively.

Figures 9 and 10 show ΔG_{rr}^{\natural} and $\Delta G_{\theta\theta}^{\natural}$, respectively, as functions of (R, Z) after the external oscillation. For the entire system, we find $\Delta G_{rr}^{\natural} \geq 0$ and $\Delta G_{\theta\theta}^{\natural} \leq 0$. At $R = D/2$ and $z = H$, $|\Delta G_{rr}^{\natural}|$ and $|\Delta G_{\theta\theta}^{\natural}|$ are largest. The spatial distributions are consistent with the residual stresses shown in Figs. 5 and 6. These results indicate that the shear strain given by Eq. (38) causes the plastic deformation following Eqs. (44) and (45), resulting in the residual stress $S_{\theta\theta} > 0$ consistent with the radial crack patterns in Fig. 1 (b).

IV. CONCLUSIONS

In this study, we numerically investigated the residual stress in a paste after rotating a cylindrical container

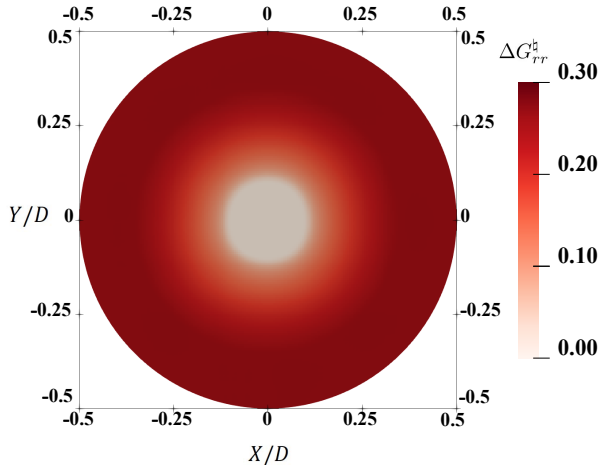


FIG. 7. Spatial distribution of ΔG_{rr}^h at $Z = 0$ after the rotation.

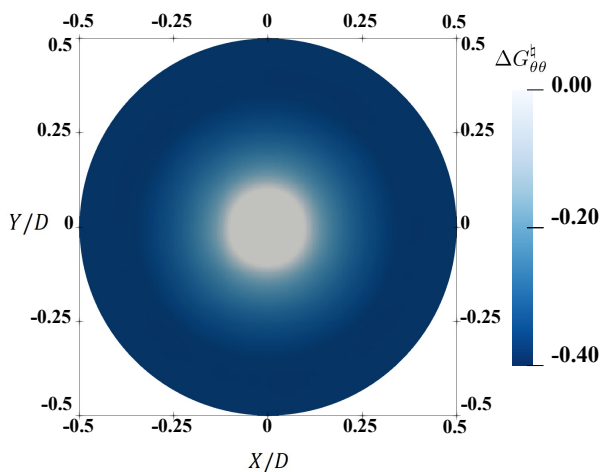


FIG. 8. Spatial distribution of $\Delta G_{\theta\theta}^h$ at $Z = 0$ after the rotation.

based on an elasto-plastic model. The tension in the circumferential direction increases after the rotation as a memory effect. The residual stress is consistent with the experimentally observed radial crack pattern after desiccation [7]. We analytically related the increase in tension to the change in the natural metric tensor characterizing plastic deformation. From the analysis of the time evolution of the natural metric tensor, we can theoretically explain the increase in tension in the circumferential direction.

In our analysis, a large plastic deformation occurs near the wall of the cylindrical container, leading to maximum residual stress at the wall. Residual stress is enhanced by

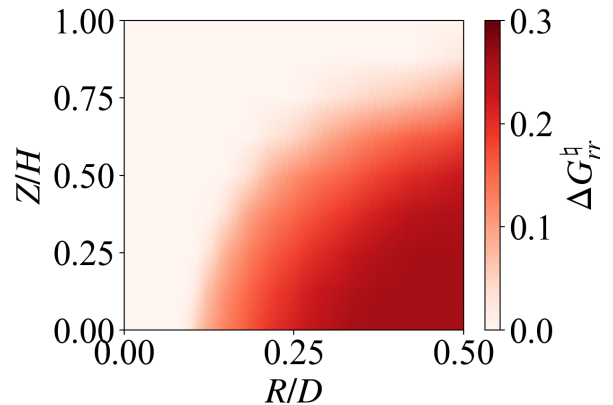


FIG. 9. Spatial distribution of ΔG_{rr}^h at $\Theta = 0$ after the rotation.

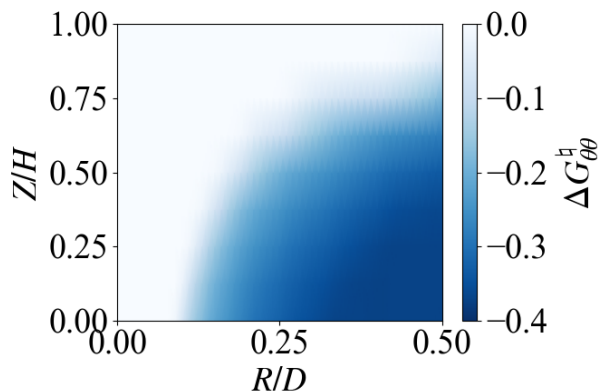


FIG. 10. Spatial distribution of $\Delta G_{\theta\theta}^h$ at $\Theta = 0$ after the rotation.

desiccation [32, 33]. Therefore, we expect that the radial crack in the experiments after desiccation is initiated at the wall boundary. However, further studies are required to confirm this.

In experiments on pastes containing magnesium carbonate hydroxide [9], radial crack patterns changed to ring patterns when a large deformation is applied. The ring crack patterns are expected to result from an increase in the residual tension in the radial direction. However, this residual stress distribution is not observed in our numerical simulations. An improvement in the elasto-plastic model will explain this behavior in the future.

ACKNOWLEDGMENTS

The authors thank T. Ooshida, Y. Motoori, and S. Goto for the fruitful discussions. This study was partially supported by JSPS KAKENHI (Grant Nos. JP21H01006 ald JP23K03248). We would like to thank Editage

(www.editage.jp) for the English language editing.

Appendix A: Approximation of left Cauchy-Green tensor

In this appendix, we derive Eqs. (39), (40), and (41). The left Cauchy-Green strain tensor \mathbf{B} given by Eq. (14) is rewritten as

$$\begin{aligned} \mathbf{B} = & g_{\natural}^{XX} \left(\frac{\partial \mathbf{r}}{\partial X} \otimes \frac{\partial \mathbf{r}}{\partial X} \right) + g_{\natural}^{XY} \left(\frac{\partial \mathbf{r}}{\partial X} \otimes \frac{\partial \mathbf{r}}{\partial Y} \right) \\ & + g_{\natural}^{XZ} \left(\frac{\partial \mathbf{r}}{\partial X} \otimes \frac{\partial \mathbf{r}}{\partial Z} \right) + g_{\natural}^{YX} \left(\frac{\partial \mathbf{r}}{\partial Y} \otimes \frac{\partial \mathbf{r}}{\partial X} \right) \\ & + g_{\natural}^{YY} \left(\frac{\partial \mathbf{r}}{\partial Y} \otimes \frac{\partial \mathbf{r}}{\partial Y} \right) + g_{\natural}^{YZ} \left(\frac{\partial \mathbf{r}}{\partial Y} \otimes \frac{\partial \mathbf{r}}{\partial Z} \right) \\ & + g_{\natural}^{ZX} \left(\frac{\partial \mathbf{r}}{\partial Z} \otimes \frac{\partial \mathbf{r}}{\partial X} \right) + g_{\natural}^{ZY} \left(\frac{\partial \mathbf{r}}{\partial Z} \otimes \frac{\partial \mathbf{r}}{\partial Y} \right) \\ & + g_{\natural}^{ZZ} \left(\frac{\partial \mathbf{r}}{\partial Z} \otimes \frac{\partial \mathbf{r}}{\partial Z} \right). \end{aligned} \quad (\text{A1})$$

Here, $\frac{\partial \mathbf{r}}{\partial X_i}$ is written as

$$\frac{\partial \mathbf{r}}{\partial X_i} = \frac{\partial R}{\partial X_i} \frac{\partial \mathbf{r}}{\partial R} + \frac{\partial \Theta}{\partial X_i} \frac{\partial \mathbf{r}}{\partial \Theta} + \frac{\partial Z}{\partial X_i} \frac{\partial \mathbf{r}}{\partial Z}. \quad (\text{A2})$$

Equation (23) gives

$$\frac{\partial R}{\partial X} = \cos \Theta \quad \frac{\partial R}{\partial Y} = \sin \Theta \quad \frac{\partial R}{\partial Z} = 0, \quad (\text{A3})$$

$$\frac{\partial \Theta}{\partial X} = -\frac{\sin \Theta}{R} \quad \frac{\partial \Theta}{\partial Y} = \frac{\cos \Theta}{R} \quad \frac{\partial \Theta}{\partial Z} = 0 \quad (\text{A4})$$

$$\frac{\partial Z}{\partial X} = 0 \quad \frac{\partial Z}{\partial Y} = 0 \quad \frac{\partial Z}{\partial Z} = 1. \quad (\text{A5})$$

From Eq. (38), we obtain

$$\frac{\partial \mathbf{r}}{\partial R} = \mathbf{e}_r, \quad \frac{\partial \mathbf{r}}{\partial \Theta} = R \mathbf{e}_\theta, \quad \frac{\partial \mathbf{r}}{\partial Z} = R(\partial_Z \varphi) \mathbf{e}_\theta + \mathbf{e}_z. \quad (\text{A6})$$

Substituting Eqs. (A3)-(A6) into Eq. (A2), we obtain

$$\frac{\partial \mathbf{r}}{\partial X} = \cos \Theta \mathbf{e}_r - \sin \Theta \mathbf{e}_\theta, \quad (\text{A7})$$

$$\frac{\partial \mathbf{r}}{\partial Y} = \sin \Theta \mathbf{e}_r + \cos \Theta \mathbf{e}_\theta, \quad (\text{A8})$$

$$\frac{\partial \mathbf{r}}{\partial Z} = R(\partial_Z \varphi) \mathbf{e}_\theta + \mathbf{e}_z. \quad (\text{A9})$$

The inverse matrix \mathbf{g}_{\natural} in Eq. (A1) is represented as

$$\mathbf{g}_{\natural} = \mathbf{Q}^T \mathbf{G}_{\natural} \mathbf{Q}, \quad (\text{A10})$$

where \mathbf{G}_{\natural} satisfies

$$\mathbf{G}_{\natural} \mathbf{G}^{\natural} = \mathbb{1}. \quad (\text{A11})$$

Considering a small deformation of $\varphi \ll 1$, \mathbf{G}_{\natural} can be approximated as

$$\mathbf{G}_{\natural} \simeq \begin{pmatrix} 1 - \Delta G_{rr}^{\natural} & -\gamma & -\delta \\ -\gamma & 1 - \Delta G_{\theta\theta}^{\natural} & -\epsilon \\ -\delta & -\epsilon & 1 + \Delta G_{rr}^{\natural} + \Delta G_{\theta\theta}^{\natural} \end{pmatrix}. \quad (\text{A12})$$

Substituting Eq. (A12) into Eq. (A10), (g_{\natural}^{ij}) is written as

$$g_{\natural}^{XX} = (1 - \Delta G_{rr}^{\natural}) \cos^2 \theta + (1 - \Delta G_{\theta\theta}^{\natural}) \sin^2 \theta + 2\gamma \sin \theta \cos \theta, \quad (\text{A13})$$

$$g_{\natural}^{YY} = (1 - \Delta G_{rr}^{\natural}) \sin^2 \theta + (1 - \Delta G_{\theta\theta}^{\natural}) \cos^2 \theta - 2\gamma \sin \theta \cos \theta, \quad (\text{A14})$$

$$g_{\natural}^{ZZ} = 1 + \Delta G_{rr}^{\natural} + \Delta G_{\theta\theta}^{\natural}, \quad (\text{A15})$$

$$g_{\natural}^{XY} = g_{\natural}^{YX} = (\Delta G_{\theta\theta}^{\natural} - \Delta G_{rr}^{\natural}) \sin \theta \cos \theta - \gamma(\cos^2 \theta - \sin^2 \theta), \quad (\text{A16})$$

$$g_{\natural}^{YZ} = g_{\natural}^{ZY} = -\delta \sin \theta - \epsilon \cos \theta, \quad (\text{A17})$$

$$g_{\natural}^{ZX} = g_{\natural}^{XZ} = -\delta \cos \theta + \epsilon \sin \theta. \quad (\text{A18})$$

Substituting Eq. (A1) with these equations and Eqs. (A7)-(A9) into Eq. (33), we obtain

$$B_{rr} = (1 - \Delta G_{rr}^{\natural}) \cos^2 \varphi + (1 - \Delta G_{\theta\theta}^{\natural}) \sin^2 \varphi + 2\gamma \sin \varphi \cos \varphi, \quad (\text{A19})$$

$$\begin{aligned} B_{\theta\theta} = & (1 - \Delta G_{rr}^{\natural}) \sin^2 \varphi + (1 - \Delta G_{\theta\theta}^{\natural}) \cos^2 \varphi \\ & - 2\gamma \sin \varphi \cos \varphi \\ & - 2(\delta \sin \varphi + \epsilon \cos \varphi) R(\partial_Z \varphi) \\ & + (1 + \Delta G_{rr}^{\natural} + \Delta G_{\theta\theta}^{\natural}) R^2 (\partial_Z \varphi)^2, \end{aligned} \quad (\text{A20})$$

$$B_{zz} = 1 + \Delta G_{rr}^{\natural} + \Delta G_{\theta\theta}^{\natural}. \quad (\text{A21})$$

Neglecting the higher-order terms of ΔG_{rr}^{\natural} , $\Delta G_{\theta\theta}^{\natural}$, γ , δ , ϵ , and φ from these equations, we obtain Eqs. (39), (40), and (41).

Appendix B: Time evolution of the natural metric tensor

In this appendix, we derive Eqs. (44) and (45). From Eq. (A10), \mathbf{G}_{\natural} is represented as

$$\mathbf{G}_{\natural} = \mathbf{Q} \mathbf{g}_{\natural} \mathbf{Q}^T. \quad (\text{B1})$$

By differentiating this equation by t , we obtain

$$\partial_t \mathbf{G}_{\natural} = \mathbf{Q} (\partial_t \mathbf{g}_{\natural}) \mathbf{Q}^T + (\partial_t \mathbf{Q}) \mathbf{Q}^T \mathbf{G}_{\natural} + \{(\partial_t \mathbf{Q}) \mathbf{Q}^T \mathbf{G}_{\natural}\}^T. \quad (\text{B2})$$

Here, we introduce

$$\mathbf{G} = \mathbf{Q} \mathbf{g} \mathbf{Q}^T \quad (\text{B3})$$

and its inverse

$$\mathbf{G}^{-1} = \mathbf{Q}\mathbf{g}^{-1}\mathbf{Q}^T. \quad (\text{B4})$$

From Eq. (18), we obtain

$$\mathbf{Q}(\partial_t \mathbf{g}_{\mathfrak{h}}) \mathbf{Q}^T = \tau^{-1} (\Gamma \mathbf{G}^{-1} - \mathbf{G}_{\mathfrak{h}}). \quad (\text{B5})$$

Using Eqs. (35) and (A12), the second and third terms on the right-hand side of Eq. (B2) are written as

$$(\partial_t \mathbf{Q}) \mathbf{Q}^T \mathbf{G}_{\mathfrak{h}} + \{(\partial_t \mathbf{Q}) \mathbf{Q}^T \mathbf{G}_{\mathfrak{h}}\}^T = \tilde{\mathbf{G}}_{\mathfrak{h}} \partial_t \varphi \quad (\text{B6})$$

with

$$\tilde{\mathbf{G}}_{\mathfrak{h}} = \begin{pmatrix} -2\gamma & \Delta G_{rr}^{\mathfrak{h}} - \Delta G_{\theta\theta}^{\mathfrak{h}} & -\epsilon \\ \Delta G_{rr}^{\mathfrak{h}} - \Delta G_{\theta\theta}^{\mathfrak{h}} & 2\gamma & \delta \\ -\epsilon & \delta & 0 \end{pmatrix}. \quad (\text{B7})$$

Substituting Eqs. (B5) and (B6) into Eq. (B2), we obtain

$$\partial_t \mathbf{G}_{\mathfrak{h}} - \tilde{\mathbf{G}}_{\mathfrak{h}} \partial_t \varphi = \tau^{-1} (\Gamma \mathbf{G}^{-1} - \mathbf{G}_{\mathfrak{h}}). \quad (\text{B8})$$

From Eqs. (A7), (A8), and (A9) with Eq. (12), the natural metric tensor is given by

$$\begin{aligned} \mathbf{g} &= \begin{pmatrix} g_{XX} & g_{XY} & g_{XZ} \\ g_{YX} & g_{YY} & g_{YZ} \\ g_{ZX} & g_{ZY} & g_{ZZ} \end{pmatrix} \\ &= \begin{pmatrix} 1 & 0 & -R(\partial_Z \varphi) \sin \Theta \\ 0 & 1 & R(\partial_Z \varphi) \cos \Theta \\ -R(\partial_Z \varphi) \sin \Theta & R(\partial_Z \varphi) \cos \Theta & 1 + R^2(\partial_Z \varphi)^2 \end{pmatrix}. \end{aligned} \quad (\text{B9})$$

Substituting Eq. (B9) into Eq. (B3) with Eq. (35), we obtain

$$\mathbf{G} = \begin{pmatrix} 1 & 0 & R(\partial_Z \varphi) \sin \varphi \\ 0 & 1 & R(\partial_Z \varphi) \cos \varphi \\ R(\partial_Z \varphi) \sin \varphi & R(\partial_Z \varphi) \cos \varphi & 1 + R^2(\partial_Z \varphi)^2 \end{pmatrix}. \quad (\text{B10})$$

The inverse matrix \mathbf{G}^{-1} is approximately obtained from Eq. (B10) as

$$\mathbf{G}^{-1} \simeq \begin{pmatrix} 1 & 0 & -R\varphi(\partial_Z \varphi) \\ 0 & 1 + R^2(\partial_Z \varphi)^2 & -R(\partial_Z \varphi) \\ -R\varphi(\partial_Z \varphi) & -R(\partial_Z \varphi) & 1 \end{pmatrix}. \quad (\text{B11})$$

The coefficient Γ given by Eq. (19) can be expressed as follows:

$$\Gamma = \frac{3}{\text{tr}(\mathbf{g}^{-1}\mathbf{g}^{\mathfrak{h}})} = \frac{3}{\text{tr}(\mathbf{G}^{-1}\mathbf{G}^{\mathfrak{h}})}. \quad (\text{B12})$$

Substituting Eqs. (36) and (B11) into Eq. (B12), Γ is approximately represented as

$$\Gamma \simeq 1 - \frac{1}{3} R^2 (\partial_Z \varphi)^2. \quad (\text{B13})$$

Using Eqs. (B11) and (B13), we obtain

$$\Gamma \mathbf{G}^{-1} \simeq \begin{pmatrix} 1 - \frac{1}{3} R^2 (\partial_Z \varphi)^2 & 0 & -R\varphi(\partial_Z \varphi) \\ 0 & 1 + \frac{2}{3} R^2 (\partial_Z \varphi)^2 & -R(\partial_Z \varphi) \\ -R\varphi(\partial_Z \varphi) & -R(\partial_Z \varphi) & 1 - \frac{1}{3} R^2 (\partial_Z \varphi)^2 \end{pmatrix}. \quad (\text{B14})$$

Substituting Eqs. (36), (B7), (B14) into Eq. (B8), we derive the time evolution equations for ΔG_{rr} and $\Delta G_{\theta\theta}$ as Eqs. (44) and (45).

-
- [1] L. Goehring, A. Nakahara, T. Dutta, S. Kitsunozaki, and S. Tarafdar, *Desiccation Cracks and their Patterns* (Wiley, 2015).
- [2] E. M. Kindle, Some factors affecting the development of mud-cracks, *J. Geol.* **25**, 135 (1917).
- [3] A. Groisman and E. Kaplan, An experimental study of cracking induced by desiccation, *EPL* **25**, 415 (1994).
- [4] S. Bohn, L. Pauchard, and Y. Couder, Hierarchical crack pattern as formed by successive domain divisions., *Phys. Rev. E* **71**, 046214 (2005).
- [5] K. A. Shorlin, J. R. de Bruyn, M. Graham, and S. W. Morris, Development and geometry of isotropic and directional shrinkage-crack patterns, *Phys. Rev. E* **61**, 6950 (2000).
- [6] L. Goehring, R. Conroy, A. Akhter, W. J. Clegg, and A. F. Routh, Evolution of mud-crack patterns during repeated drying cycles, *Soft Matter* **6**, 3562 (2010).
- [7] A. Nakahara and Y. Matsuo, Imprinting memory into paste and its visualization as crack patterns in drying process, *J. Phys. Soc. Jpn.* **74**, 1362 (2005).
- [8] A. Nakahara and Y. Matsuo, Imprinting memory into paste to control crack formation in drying process, *J. Stat. Mech: Theory Exp.* **2006**, P07016 (2006).
- [9] A. Nakahara and Y. Matsuo, Transition in the pattern of cracks resulting from memory effects in paste, *Phys. Rev. E* **74**, 045102 (2006).
- [10] Y. Matsuo and A. Nakahara, Effect of interaction on the formation of memories in paste, *J. Phys. Soc. Jpn.* **81**, 024801 (2012).
- [11] H. Nakayama, Y. Matsuo, O. Takeshi, and A. Nakahara, Position control of desiccation cracks by memory effect and faraday waves, *Eur. Phys. J. E* **36**, 1 (2013).
- [12] D. Mal, S. Sinha, S. Mitra, and S. Tarafdar, Formation of crack networks in drying laponite films, *Physica A* **346**, 110 (2005).
- [13] T. Khatun, T. Dutta, and S. Tarafdar, Crack formation under an electric field in droplets of laponite gel: Memory effect and scaling relations, *Langmuir* **29**, 15535 (2013).
- [14] L. Pauchard, F. Elias, P. Boltzenhagen, A. Cebers, and J. C. Bacri, When a crack is oriented by a magnetic field,

- Phys. Rev. E **77**, 021402 (2008).
- [15] A. T. Ngo, J. Richardi, and M. P. Pileni, Do directional primary and secondary crack patterns in thin films of maghemite nanocrystals follow a universal scaling law?, J. Phys. Chem. B **112**, 14409 (2008).
- [16] H. Lama, V. R. Dugvala, M. G. Basavaraj, and D. K. Satapathy, Magnetic-field-driven crack formation in an evaporated anisotropic colloidal assembly, Phys. Rev. E **94**, 012618 (2016).
- [17] R. Szatmári, Z. Halász, A. Nakahara, S. Kitsunozaki, and F. Kun, Evolution of anisotropic crack patterns in shrinking material layers, Soft Matter **17**, 10005 (2021).
- [18] C. Uemura, A. Nakahara, Y. Matsuo, and T. Iwata, Transition condition between memories of vibration and flow in the memory effect of paste, Phys. Rev. E **109**, 034604 (2024).
- [19] R. Baba, K. Fujimaki, C. Uemura, Y. Matsuo, A. Nakahara, and A. Muramatsu, Assisting and eliminating memory effects of paste by adding polysaccharides, Phys. Rev. E **108**, 054602 (2023).
- [20] A. Nakahara, Y. Shinohara, and Y. Matsuo, Control of crack pattern using memory effect of paste, J. Phys. Conf. Ser. **319**, 012014 (2011).
- [21] A. Nakahara, T. Hiraoka, R. Hayashi, Y. Matsuo, and S. Kitsunozaki, Mechanism of memory effect of paste which dominates desiccation crack patterns, Philos. Trans. R. Soc. A **377**, 20170395 (2019).
- [22] S. Kitsunozaki, Fracture patterns induced by desiccation in a thin layer, Phys. Rev. E **60**, 6449 (1999).
- [23] K. B. Singh and M. S. Tirumkudulu, Cracking in drying colloidal films, Phys. Rev. Lett. **98**, 218302 (2007).
- [24] W. Man and W. B. Russel, Direct measurements of critical stresses and cracking in thin films of colloid dispersions, Phys. Rev. Lett. **100**, 198302 (2008).
- [25] Z. Halász, A. Nakahara, S. Kitsunozaki, and F. Kun, Effect of disorder on shrinkage-induced fragmentation of a thin brittle layer, Phys. Rev. E **96**, 033006 (2017).
- [26] S. Ito and S. Yukawa, Dynamical scaling of fragment distribution in drying paste, Phys. Rev. E **90**, 042909 (2014).
- [27] S. Ito and S. Yukawa, Stochastic modeling on fragmentation process over lifetime and its dynamical scaling law of fragment distribution, J. Phys. Soc. Jpn. **83**, 124005 (2014).
- [28] S. Hirobe and K. Oguni, Coupling analysis of pattern formation in desiccation cracks, Comput. Methods Appl. Mech. Eng. **307**, 470 (2016).
- [29] S. Hirobe, Numerical simulation of desiccation cracking process by weak coupling of desiccation and fracture, Int. J. GEOMATE **12**, 10.21660/2017.33.2535 (2017).
- [30] S. Hirobe and K. Oguni, Modeling and numerical investigations for hierarchical pattern formation in desiccation cracking, Physica D **359**, 29 (2017).
- [31] S. Hirobe and K. Oguni, Modeling and simulating methods for the desiccation cracking, Int. J. Comput. Methods **16**, 1840011 (2019).
- [32] S. Kitsunozaki, A. Nakahara, and Y. Matsuo, Shaking-induced stress anisotropy in the memory effect of paste, EPL **114**, 64002 (2016).
- [33] S. Kitsunozaki, A. Sasaki, A. Nishimoto, T. Mizuguchi, Y. Matsuo, and A. Nakahara, Memory effect and anisotropy of particle arrangements in granular paste, Eur. Phys. J. E **40**, 88 (2017).
- [34] M. Otsuki, Memory effect on the formation of drying cracks, Phys. Rev. E **72**, 10.1103/PhysRevE.72.046115 (2005).
- [35] T. Ooshida, Continuum theory of memory effect in crack patterns of drying pastes, Phys. Rev. E **77**, 061501 (2008).
- [36] T. Ooshida, Three-dimensional residual tension theory of nakahara effect in pastes, J. Phys. Soc. Jpn. **78**, 104801 (2009).
- [37] J. Morita and M. Otsuki, Memory effect of external oscillation on residual stress in a paste, Eur. Phys. J. E **44**, 106 (2021).
- [38] J. Marsden and T. J. R. Hughes, *Mathematical foundations of elasticity* (Dover Publications, Inc., 1994).
- [39] A. Romano and A. Marasco, *Continuum Mechanics using Mathematica®* (Springer New York, 2014).
- [40] C. Truesdell and W. Noll, *The Non-Linear Field Theories of Mechanics*, edited by S. S. Antman (Springer Berlin Heidelberg, 2004).
- [41] M. F. Beatty, Topics in finite elasticity: Hyperelasticity of rubber, elastomers, and biological tissues—with examples, Appl. Mech. Rev. **40**, 1699 (1987).
- [42] M. Destrade and G. Saccomandi, Finite amplitude elastic waves propagating in compressible solids, Phys. Rev. E **72**, 016620 (2005).
- [43] R. M. Jones, *Deformation Theory of Plasticity* (Bull Ridge Pub., 2009).